

Disruption of the European climate seasonal clock in a warming world

Christophe Cassou^{1*} and Julien Cattiaux²

Temperatures over Europe are largely driven by the strength and inland penetration of the oceanic westerly flow. The wind influence depends on season: blocked westerlies, linked to high-pressure anomalies over Scandinavia, induce cold episodes in winter¹ but warm conditions in summer^{2,3}. Here, we propose to define the onset of the two seasons as the calendar day on which the daily circulation/temperature relationship switches sign. We have assessed this meteorologically based metric using several observational data sets and we provide evidence for an earlier onset of the summer date by ~10 days between the 1960s and 2000s. Results from a climate model show that internal variability alone cannot explain this calendar advance. Rather, the earlier onset can be partly attributed to anthropogenic forcings. The modification of the zonal advection due to earlier disappearance of winter snow over Eastern Europe, which reduces the degree to which climate has continental properties, is mainly responsible for the present-day and near-future advance of the summer date in Western Europe. Our findings are in line with phenological-based trends (earlier spring events) reported for many living species over Europe^{4–6}, for which we provide an alternative interpretation to the traditionally evoked local warming effect. Based on the Representative Concentration Pathway (RCP) 8.5 scenario, which assumes that greenhouse gas emissions continue to rise throughout the twenty-first century, a summer advance of ~20 days compared with pre-industrial climate is expected by 2100, whereas no clear signal arises for winter onset.

Travelling synoptic pressure systems, or storms, account for much of the variability in European climate on timescales from days to years⁷. Their inland penetration can be simply assessed from a daily index of zonal wind averaged over Western Europe, which is strongly associated with sea-level pressure (PSL) anomalies located over Scandinavia, as expected from geostrophy (balance between the Coriolis force and the pressure gradient force). The correlation between the two daily fields is indeed equal to -0.9 (that is, ~80% of explained variance), highlighting the strong link between enhanced (slackened) westerly flows due to storm intrusion along the European oceanic flank, and negative (positive) PSL anomalies north of 55° N (Fig. 1a). Upstream from Europe, storms originate from the unstable nature of the upper-level westerly jet stream over the North Atlantic, and feed circulation patterns, or modes of variability, in which they are embedded⁸. To a great extent, their penetration over Western Europe is controlled by the third mode of large-scale atmospheric variability, traditionally extracted through a principal component analysis of anomalous PSL maps over the North Atlantic⁹ (Supplementary Fig. 1). This mode (hereafter SCAND) is characterized by a meridional seesaw⁹

pattern between Scandinavia and the southern tip of Greenland; its positive phase (high pressure over Scandinavia) corresponds to so-called 'blocked' situations where storms are deflected to the far-north subarctic region and/or develop further south in the Mediterranean Sea^{10,11}.

When describing the dynamics of the North Atlantic, winter and summer are usually treated separately to account for the seasonality in both location and strength of the mean pressure centres of action. It is particularly important for the first two modes of variability, the North Atlantic Oscillation and the East Atlantic Pattern, which depict a pronounced seasonal latitudinal migration of their anomalous cores (Supplementary Fig. 1). In contrast, the spatial structure of SCAND is fixed throughout the entire year, as is the fraction of daily zonal wind variance explained by daily PSL over Scandinavia (Supplementary Fig. 2a–c). On the basis of these dynamical properties and aiming at investigating the seasonal cycle of the European atmospheric circulation and associated heat transport, we construct a box-averaged index of continuous raw daily pressure anomalies (hereafter PSLi) over a domain that jointly matches the SCAND European core (Supplementary Fig. 1c) and the region of maximum correlation with the penetrating zonal westerly flow over Western Europe¹² (Fig. 1a).

In winter, positive values for PSLi correspond to cold conditions over most of Europe (south of 60° N, Fig. 1b). During strong events, totally blocked oceanic westerly winds allow for anomalous easterly inflow of cold and dry air masses and concomitant long-wave radiative loss due to clear-sky nights¹, therefore favouring cold waves. In summer, positive temperature anomalies are found instead, especially over Western Europe (Fig. 1c). Blocked conditions then allow for anomalous easterly advection of warmer air from the continental interior and enhanced short-wave incoming radiation at the surface due to clear-sky days, leading to heat waves. Such a seasonal reversal¹² in the circulation/temperature relationship is related to the seasonal cycle of the mean zonal temperature gradient and associated heat transport between the European continent and the near North Atlantic Ocean. Similarly to PSLi, a box-averaged index of the temperature at 2 metres (hereafter T2Mi) is calculated from raw daily anomalies over the above-defined Western Europe domain (Fig. 1) that best covers the region where the PSLi/temperature relationship switches sign between winter and summer seasons (Fig. 1b,c and Supplementary Fig. 2d–f).

The annual cycle of the relationship between atmospheric circulation and temperature is represented through the prism of a diagram referred to as the seasonal clock, based on a regression metric (Fig. 2). Moving clockwise from January to December, the monthly regression coefficients between daily PSLi and T2Mi draw an 8-shaped pattern within this conceptual view. Maximum stretching

¹CNRS-Cerfacs, UMR-5318, Climat, Environnement, Couplage et Incertitudes, 42, Avenue G. Coriolis, 31057 Toulouse, France. ²CNRS-Météo-France, UMR-3589 Centre National de Recherche Météorologique—Groupe d'Etude de l'Atmosphère Météorologique, 42, Avenue G. Coriolis, 31057 Toulouse, France. *e-mail: christophe.cassou@cerfacs.fr

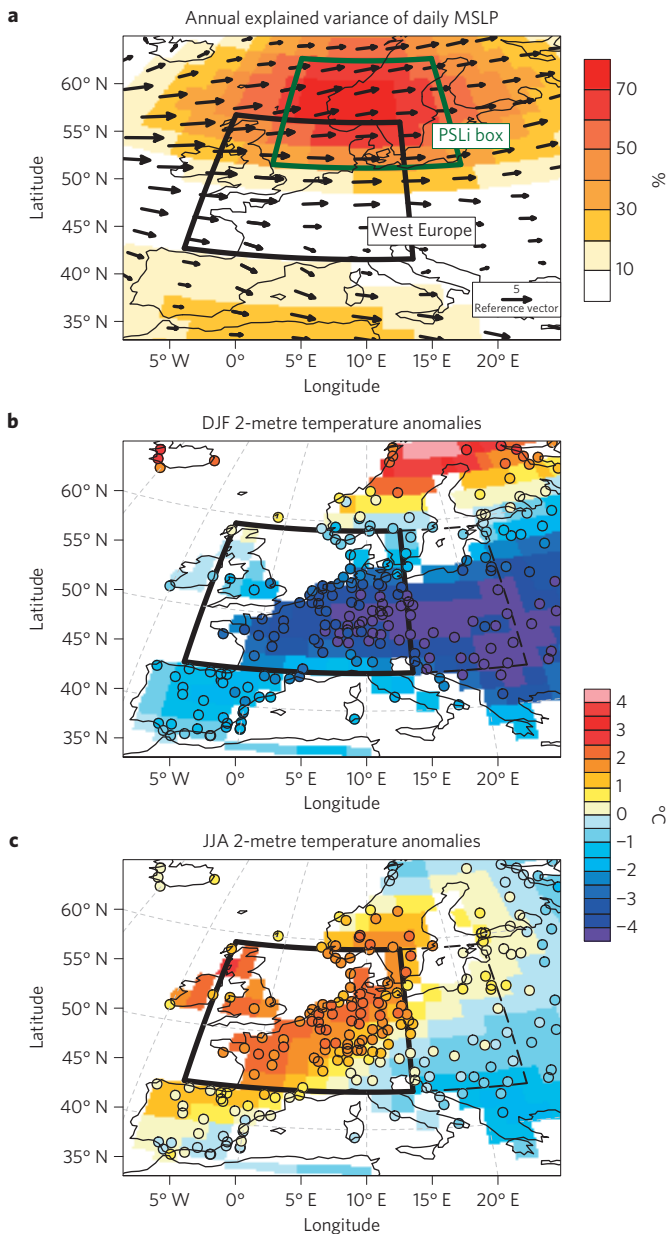


Figure 1 | Definition of the meteorological dynamical indices and assessment of the circulation-temperature seasonal relationships.

a, Fraction of variance of daily mean PSL explained by the zonal wind at 850 hPa averaged over the (5° W–15° E/45° N–58° N) West Europe domain (black rectangle). The fraction of explained variance quantifies the strength of the relationship between two variables and simply corresponds to the square of the correlation coefficient. Data are from NCEP reanalysis and the computation is made using all days over 1950–2014. Shading intervals are every 10%. Arrows represent the 850 hPa wind annual climatology. The (0° W–20° E/50° N–65° N) green rectangle represents the region selected for the PSLi computation. **b, c**, Winter (December–February) (**b**) and summer (June–August) (**c**) mean anomalous temperature at 2 metres (T2M) corresponding to days with PSLi greater than +1 s.d. Data for compositing are from NCEP reanalysis (shading) and ECA&D (ref. 13) stations (circles). Shading intervals are every 0.5 °C. The West Europe domain is then used for the T2Mi computation. The East Europe domain (dashed in **b** and **c**, (15° E–28° E/45° N–58° N)) is used later on for east–west gradients and snow cover analyses.

standing for strong PSLi/T2Mi coupling occurs for January and July where the anticorrelation and correlation values are respectively the

highest, reaching ~34% and ~28% of explained variance between the two daily indices. Maximum constricting is found in spring and autumn where the PSLi/T2Mi link progressively diminishes and eventually switches sign. Repeated calculations from several combinations of observational products over their common coverage period (here 1950–2010) provide a quantitative estimate of the observational uncertainties associated with the overall 8-shaped pattern.

The temporal evolution and associated physical mechanisms in shaping the seasonal clock, and in particular the role of anthropogenic forcings, is now investigated over 1850–2100 through a suite of Coupled Model Inter-comparison Project Phase 5 (CMIP5; ref. 14) ensemble simulations of the CNRM-CM5 (ref. 15) model. We a priori verified from so-called historical experiments (hereafter HIST) over 1950–2010 that the model performs reasonably well in reproducing the observed SCAND mode that inspired the PSLi definition, as well as the amplitude and seasonal cycle of the observed relationship between PSLi and T2Mi (Supplementary Fig. 3). We then compared the pre-industrial climate seasonal clock with the late twenty-first century clock based on projections under a high-carbon emission scenario (hereafter RCP8.5, Fig. 2b). The upper lobe of the 8-shaped pattern undergoes a significant contraction in RCP8.5, which features a considerable decrease in the circulation/temperature relationship over Western Europe in winter. The lower lobe for summer months exhibits the opposite. The largest changes are found at the end of the winter season, the absolute value of the regression coefficients being reduced by more than half in February and March, whereas the summer dynamics starts earlier in April and gets stronger throughout the entire season. No significant modifications are found from September to December.

The loss in regression between PSLi and T2Mi in winter is mostly explained by the reduction of both the variance (–23%) and the skewness (–56%) of the daily temperature probability density function (PDF), at the end of the twenty-first century¹⁶, whereas the counterpart pressure PDF is not significantly altered (Fig. 3a and Supplementary Fig. 4). Such a reduction of T2Mi statistics has been mostly attributed to the diminution of the mean zonal temperature gradients over Europe¹⁷ as climate is warming. We argue here that it is important to treat the western and eastern sides of the European domain separately for a more precise mechanistic interpretation. Even if the atmospheric flow does not undergo any major change, as in CNRM-CM5 projections (unchanged PSLi PDF, Supplementary Fig. 4a), the efficiency of the westerly advection of oceanic air masses is reduced owing to the slackening of the land–sea contrast¹⁸ (Fig. 3b). This explains the decrease in the upper-left quarter of the PSLi/T2Mi bivariate PDF (Fig. 3a), that is, why mild winter days associated with zonal flows warm less than the mean. However, land–sea contrast cannot explain the diminution in the lower-right quarter that is indicative for less severe cold events during blocking circulations (regardless of mean warming). This diminution is rather due to the considerable reduction of the temperature gradient between Eastern and Western Europe (Fig. 3b), making anomalous easterly advection of continental cold air masses less efficient. In summer, both land–sea and east–west contrast-related advection mechanisms also play a role, but with opposite signs because of the seasonal reversal of the zonal gradients (Fig. 3b). This therefore leads to enhance the variance of the daily temperature PDF^{19,20} (Fig. 3c), again regardless of significant changes in the PSLi distribution as found in CNRM-CM5 (Supplementary Fig. 4b,d). Interestingly, the variance disruption for summer temperature (Fig. 3c) is less dependent on the sign of PSLi, that is, on atmospheric circulation, than in winter (Fig. 3a), which is supportive for the existence of additional factors²¹ whose mean changes locally interact with temperature (for example, soil moisture^{20–22}).

Identification of the timing of the seasons traditionally relies on either the exceedance of fixed temperature thresholds²³, or the

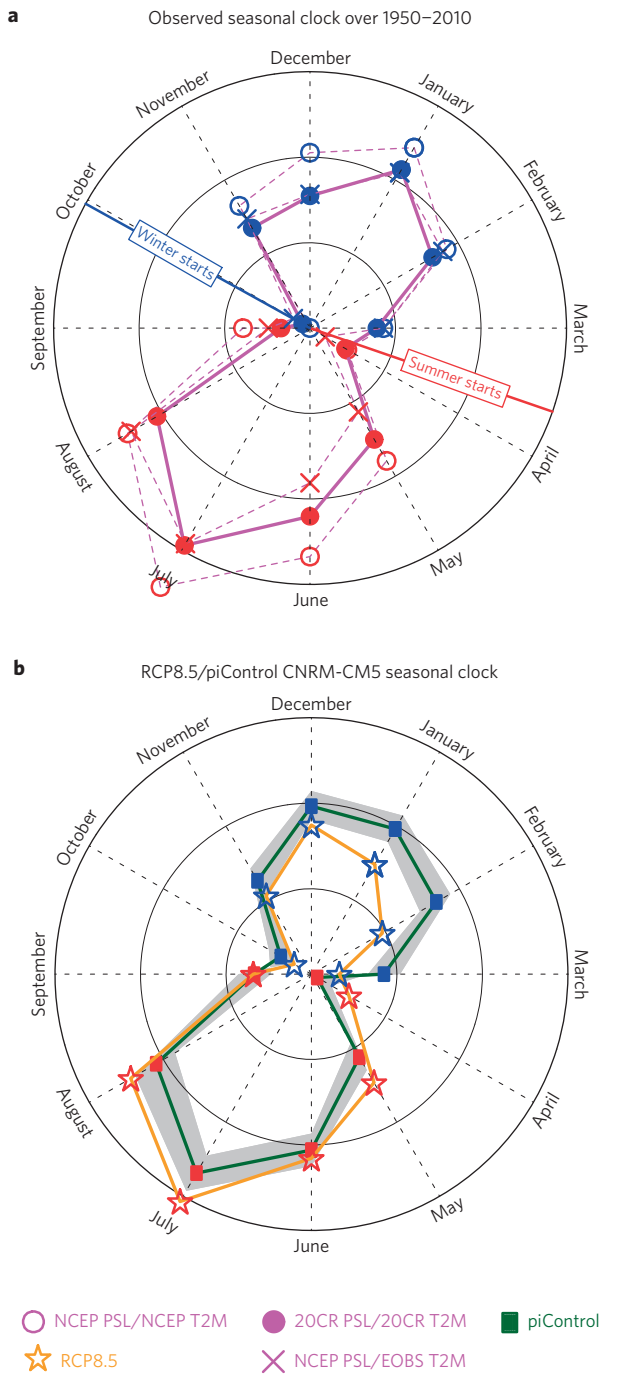


Figure 2 | Seasonal clocks. **a**, Seasonal clock of the PSLi/T2Mi relationship. For simplicity, calendar years of 360 days are divided into 12 equal 30-day months over 1950–2010 for which regression coefficients between daily PSLi and T2Mi are reported. The distance to the clock centre and the colour represent their amplitude and sign respectively. Solid concentric circles interval is $0.66\text{ }^{\circ}\text{C}/10\text{ hPa}$. Computations from several combinations of data sets (EOBS high-resolution gridded product, NCEP and NOAA-20CR reanalyses) for both PSLi and T2Mi are shown. **b**, Seasonal clock for the pre-industrial (dark green) and late twenty-first century (orange) periods assessed from the CNRM-CM5 so-called piControl 850-year-long experiment (external forcings including greenhouse gases, aerosols, solar and volcanic activities fixed to their 1850 estimates; squares) and from five members of RCP8.5 projections (stars) over 2070–2100. Grey shading represents the 5–95% confidence interval of the regression coefficients assessed from 1,000 random drawings of five 30-year periods in piControl averaged to match the five-member ensemble mean.

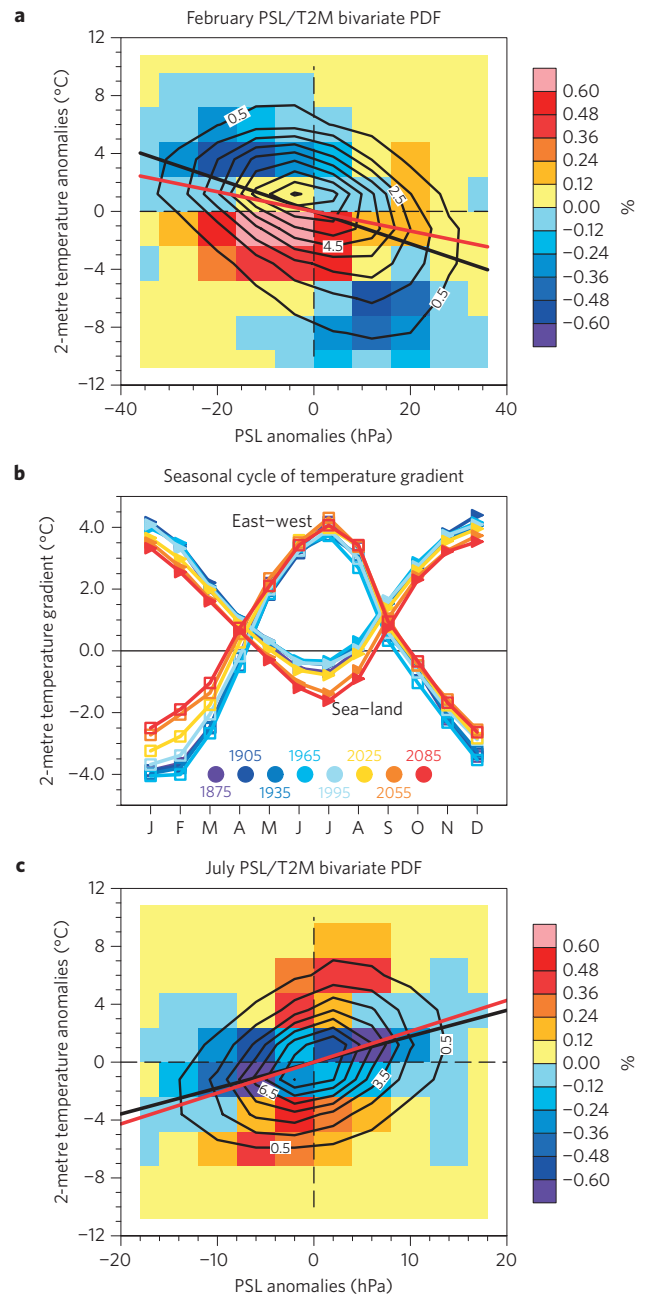


Figure 3 | Changes in the statistical distribution of daily pressure and temperature anomalies over Europe at the end of the twenty-first century based on the RCP8.5 emission scenario. **a**, February bivariate PSLi and T2Mi PDFs from piControl (contour) and RCP8.5-piControl differences (shading); contour interval is 1% and RCP8.5 anomalies have been re-centred before computing the PDF difference. The regression lines are shown in black (red) for piControl (RCP8.5). **b**, Seasonal cycle for sea-land contrast (triangle) and for the difference between T2Mi and the equivalent 2-metre temperature index over East Europe (square), computed for each month, over successive 30-year periods from 1850 (purple) to 2100 (red) centred on the date provided at the bottom. Sea/land points correspond to the ones included in the West Europe domain (see Fig. 1a for the domain description). **c**, The same as in **a**, but for July.

local determination of the phase and amplitude of the annual cycle in surface temperature^{24,25}. The former method is very sensitive to background changes and has been extensively used to explain trends in phenology known to be very responsive to temperature raw values²⁶. The latter makes it possible to disentangle phase shifts

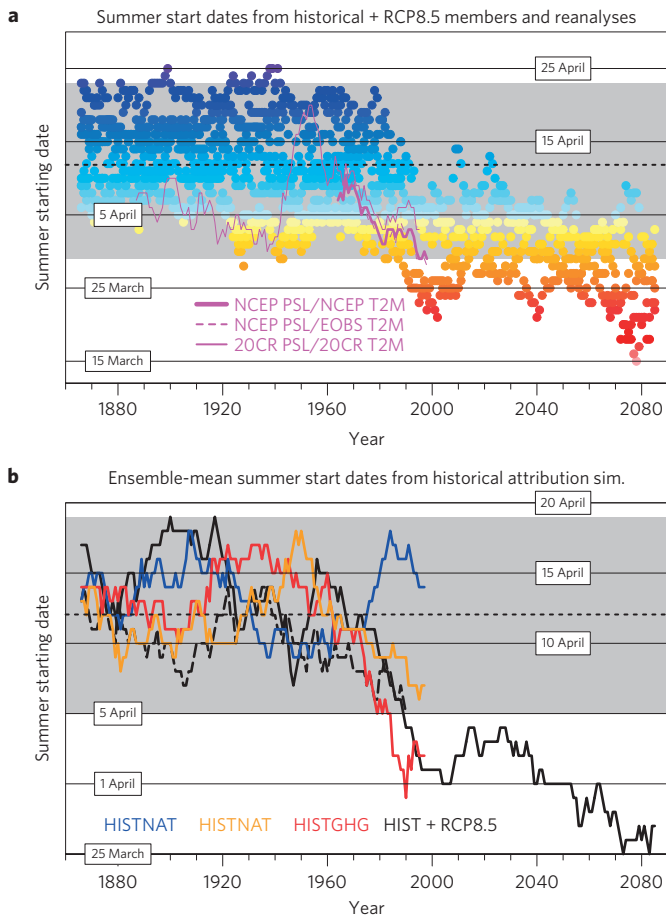


Figure 4 | Calendar change of the date of the summer onset under warming climate. **a**, Temporal evolution of the summer starting date from observational data sets (magenta curves and labels) and from historical and scenario individual ensemble members (dots) computed over running 30-year periods. Blue (red) colour of the dot (ten per year from ten available historical simulations over 1850–2012, five from five RCP8.5 ones after 2012) represents later (earlier) summer starting dates given by thin horizontal lines. The range of variability from pure internal dynamics as computed from 1,000 random drawings of 30-yr period from piControl is represented in grey (5th and 95th percentile); the mean piControl summer starting date is superimposed (thick dashed). Formal detection is obtained when the index gets outside the grey envelope. **b**, Ensemble-mean summer starting dates from five-member attribution experiments where external forcings are applied individually over the historical period, namely natural (solar + volcanoes) forcing alone (HISTNAT, blue), anthropogenic (GHG + aerosols) alone (HISTANT, orange) and GHG alone (HISTGHG, red). For HIST (black), because of ten-member availability over 1850–2012, the complementary five-member estimate is provided (dashed line). Grey shading is computed here from 1,000 random drawings of five 30-year periods in piControl averaged to match the five-member ensemble mean.

and mean changes in the annual cycle. However, both methods rely solely on local temperature modifications to evaluate seasonal shifts. Here we propose instead an objective weather-based definition of the beginning of summer and winter seasons as the date on which the regression between PSLi and T2Mi crosses zero in the course of the seasonal clock (Fig. 2). This consequently assumes that only two seasons exist per se over Europe based on the intrinsic properties of the annual cycle of the atmospheric dynamics and associated heat transport: a winter-type season, during which blocked westerlies induce cold anomalies, and a summer-type season, during which these induce warm anomalies.

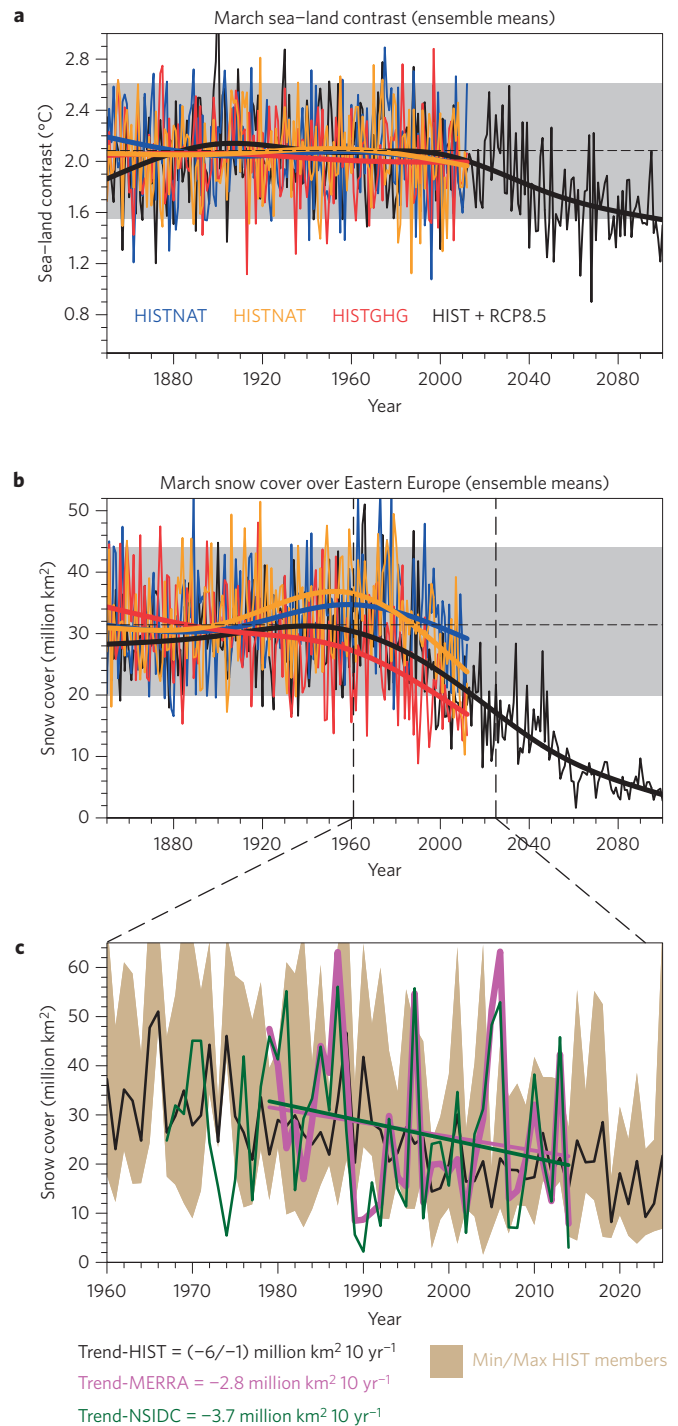


Figure 5 | Physical processes involved in the summertime seasonal shift. **a, b**, Temporal evolution of March, sea-land contrast (°C) (**a**) and snow cover (million km²) over the East Europe domain (Fig. 1b,c) (**b**) for all ensemble means of attribution runs (colours) and concatenated historical and RCP8.5 runs (black). Internal variability (grey shading) is assessed as in Fig. 3b. **c**, Zoom over the 1960–2025 period for which two observational estimates of March snow cover from MERRA reanalysis (magenta from 1979) and blended surface/satellite products²⁹ from NSIDC (green from 1967) are compared to the ten-member HIST Min/Max envelope in brown shading. To account for different box-averaged surface due to different grids, means for MERRA and NSIDC indices have been calibrated to fit the (1979–2014) CNRM-CM5 mean. Ensemble mean for HIST is over plotted (black series). Trends for observations over the common 1979–2014 period are given at the bottom together with the range estimated from the HIST ensemble.

Applying the metric to observations shows that summer in Western Europe begins on 5 April on average over 1950–2010 and about ~10 days earlier in the 2000s than in the 1960s (Fig. 4a). Beyond the mean timing, the trend in summer onset is very well replicated in HIST at about the same rate (~–2.5 days per decade over the same period). A very sharp drop-off occurs from the 1960s onwards in all of the members of the model ensemble and the most recent calendar advance (30-year period centred around 2000) is just above that expected solely from internal variability estimated from the 850-year-long pre-industrial control experiment. Such a trend is mostly interpreted, based on so-called attribution ensemble simulations, as the imprint of increased greenhouse gas concentration whose warming effect is mitigated by anthropogenic aerosols and natural forcings (Fig. 4b). Under the RCP8.5 scenario, the calendar advance is expected to continue, leading ultimately to an average advance of the summer date of ~20 days by the end of the twenty-first century, namely 25 March instead of 12 April (mean summer starting date for the pre-industrial climate conditions, Fig. 4b). Before the 1960s when external forcings are weak, all of the attribution experiments are dominated by internal low-frequency fluctuations linked, to some extent, to the model Atlantic Multidecadal Oscillation, which controls most of the spread in HIST (not shown) and whose signature is not completely cancelled out here because of the limited number of members in the model ensemble (Fig. 4a). Note that earlier summer onsets are found in the NOAA-20CR atmospheric reanalysis in the 1920–1930s in contrast to the 1950–1960s (Fig. 4a); this would be consistent with the temporal evolution of the observed Atlantic Multidecadal Oscillation and associated influence of seasonal shift²⁷ combined with the mid-century forcing by aerosols (Fig. 4b) due to European industrialization. The sparseness of assimilated observations that constrain the model atmosphere in the reanalysis product though requires extreme caution in the interpretation of these results, even if plant phenological records and reconstructions are also suggestive for earlier spring events²⁸ in the early twentieth century.

The reduction of land–sea contrast is not responsible for the detectable present-day summer calendar advance in CNRM-CM5. In March (Fig. 5a) and April (not shown) when the seasonal transition occurs, this parameter is found to be insensitive to any external forcings before the 2030s, a decade from which it undergoes a slow decrease due to accelerating continental warming locally over Western Europe (not shown). Earlier summer starting dates are rather connected to the continental east–west contrast whose maximum alteration is found for winter months (December–March, Fig. 3b). The greatest rate of change is occurring at the very present time, and the current east–west contrast slackening is tightly linked to the fast ongoing snow melt over Eastern Europe, especially in March (Fig. 5b). This leads to an amplification of the current warming both locally due to surface albedo perturbation¹⁹ and remotely due to milder air advection from the east when blocked westerly circulation occurs.

The evolving response of the March snow cover over Eastern Europe, as simulated in the attribution ensemble (Fig. 5b), is consistent with the corresponding changes in the modelled summer starting dates over Western Europe. As illustrated in CNRM-CM5, fast ongoing decrease in snow cover is also measurable at present in the observational record as estimated from several products and despite very pronounced interannual variability (Fig. 5c). A decrease in snow cover of about 3 million km² per decade is observed over 1979–2014, a trend that falls within the range given by the HIST ensemble (–6 to –1 million km² per decade).

Numerous analyses compiling systematic and comprehensive phenological network data sets of thousands of observational series of plants and animals species have demonstrated an earlier onset of spring events (budburst, flowering, and so on) with an average advance of about ~2.5 days per decade^{4–6,26,28,30} over Europe (see

Supplementary Fig. 5 for specific examples from indices based on flowering dates of cherry and apple trees and budburst of beech and Riesling grapes). Such a trend is consistent with the evolution of summer timing determined here from our approach, which consequently provides a valuable extension and additional physical insight in interpreting the recent phenological changes. Our findings are indicative that those may not be simply due to the rise of the local mean temperature as a direct response to anthropogenic forcing and/or decrease of local snow pack, as generally assumed^{26,28,30}, but can also be explained indirectly by the alteration of the intrinsic dynamical relationship between atmospheric circulation and temperature anomalies through differential warming rates. In other words, what matters is not only the mean warming per se but also its large-scale and non-uniform spatial fingerprint. In Europe, the latter is largely explained by the progressive snow-cover decline in the east, which locally causes more rapid warming, and which remotely affects Western Europe through altered heat advection when easterly events occur. It is therefore difficult without dedicated model experiments to clearly partition the documented changes between pure dynamical and thermal influences because the dynamics, even without wind circulation changes such as in CNRM-CM5, is important to export the spatial asymmetry of the thermal responses through nonlinear cross-product wind temperature terms.

Note that according to our meteorological definition of the seasons based on the intrinsic feature of the European weather, namely the annual cycle of the temperature/circulation relationship, the rate of change of the summer onset dates seems to be maximum around now in line with the ongoing rapid observed snow melt over Eastern Europe (Figs 4 and 5). This would imply that we might not expect much more pronounced change in summer onset dates in the future, even with further warming, because most of the snow in March and April that controls part of the timing of the season through anomalous advection will have disappeared in the near term (Fig. 5b). Interestingly, results are inconclusive for changes in the winter onset when assessed from our meteorological approach; no detectable trend can be found over 1850–2100 despite the fact that the mean climate is warming (Supplementary Fig. 6). Note that snow over Europe is not yet present in September/October when the summer-to-winter shift happens. This is again consistent with phenological markers (for example, leaf colouring/fall) that do not provide any consensual sign for lateness of autumn events over Western Europe^{4–6}.

Received 23 April 2015; accepted 25 February 2016;
published online 4 April 2016

References

- Sillmann, J., Croci-Maspoli, M., Kallache, M. & Katz, R. Extreme cold winter temperatures in Europe under the influence of North Atlantic atmospheric blocking. *J. Clim.* **24**, 5899–5913 (2012).
- Cassou, C., Terray, L. & Philips, A. S. Tropical influence on European heatwaves. *J. Clim.* **18**, 2805–2811 (2005).
- Schneider, A. *et al.* Large scale flow and the long-lasting blocking high over Russia: summer 2010. *Mon. Weath. Rev.* **140**, 2967–2981 (2012).
- Menzel, A. *et al.* European phenological response to climate change matches the warming pattern. *Glob. Change Biol.* **12**, 1969–1976 (2006).
- Thackeray, S. J. *et al.* Trophic level asynchrony in rates of phenological change for marine, freshwater and terrestrial environments. *Glob. Change Biol.* **16**, 3304–3313 (2010).
- Settele, J. *et al.* in *IPCC Climate Change 2014: Impacts, Adaptation and Vulnerability* 271–359 (IPCC, Cambridge Univ. Press, 2014).
- Chang, E. K. M., Lee, S. & Swanson, K. L. Storm track dynamics. *J. Clim.* **15**, 2163–2183 (2002).
- Wettstein, J. & Wallace, J. M. Observed patterns of month-to-month storm-track variability and their relationship to the background flow. *J. Atmos. Sci.* **67**, 1420–1437 (2010).
- Barnston, A. G. & Livezey, R. E. Classification, seasonality and persistence of low-frequency atmospheric circulation patterns. *Mon. Weath. Rev.* **115**, 1083–1126 (1987).

10. Rex, D. F. Blocking action in the middle troposphere and its effect upon regional climate. II. The climatology of blocking action. *Tellus* **2**, 275–301 (1950).
11. Pelly, J. L. & Hoskins, B. J. A new perspective on blocking. *J. Atmos. Sci.* **60**, 743–755 (2003).
12. Slonosky, V. C., Jones, P. D. & Davies, T. D. Atmospheric circulation and surface temperature in Europe from the 18th century to 1995. *Int. J. Climatol.* **21**, 63–75 (2001).
13. Haylock, M. R. *et al.* A European daily high-resolution gridded dataset of surface temperature and precipitation. *J. Geophys. Res.* **113**, D20119 (2008).
14. Taylor, K. E., Stouffer, R. J. & Meehl, G. A. An overview of CMIP5 and the experiment design. *Bull. Am. Meteorol. Soc.* **93**, 485–498 (2012).
15. Voldoire, A. *et al.* The CNRM-CM5.1 global climate model: description and basic evaluation. *Clim. Dynam.* **40**, 2091–2121 (2013).
16. Collins, M. *et al.* in *IPCC Climate Change 2013: The Physical Science Basis* 1029–1136 (IPCC, Cambridge Univ. Press, 2013).
17. De Vries, H., Haarsma, R. J. & Hazelger, W. Western European cold spells in current and future climate. *Geophys. Res. Lett.* **39**, L04706 (2012).
18. Sutton, R. T., Dong, B. & Gregory, J. M. Land/sea warming ratio in response to climate change: IPCC AR4 model results and comparison with observations. *Geophys. Res. Lett.* **34**, L02701 (2007).
19. Fischer, E. M., Lawrence, D. M. & Sanderson, B. M. Quantifying uncertainties in projections of extremes—a perturbed land surface parameter experiment. *Clim. Dynam.* **37**, 1381–1398 (2011).
20. Fischer, E. M., Rajczak, J. & Schär, C. Changes in European summer temperature variability revisited. *Geophys. Res. Lett.* **39**, L19702 (2012).
21. Boé, J. & Terray, L. Land–sea contrast, soil–atmosphere and cloud–temperature interactions: interplays and roles in future summer European climate change. *Clim. Dynam.* **42**, 683–699 (2013).
22. Cattiaux, J., Douville, H., Schoetter, R., Parey, S. & Yiou, P. Projected increase in diurnal and interdiurnal variations of European summer temperatures. *Geophys. Res. Lett.* **42**, 899–907 (2015).
23. Kirbyshire, A. L. & Bigg, G. R. Is the onset of English summer advancing? *Climatic Change* **100**, 419–431 (2010).
24. Stine, A. P., Huyberts, P. & Fung, I. Changes in the phase of the annual cycle of surface temperature. *Nature* **457**, 435–440 (2009).
25. Trenberth, K. E. What are the seasons? *Bull. Am. Meteorol. Soc.* **64**, 1276–1282 (1983).
26. Sparks, T. & Menzel, A. Observed changes in seasons: an overview. *Int. J. Climatol.* **22**, 1715–1725 (2002).
27. Pena-Ortiz, C., Barriopedro, D. B. & Garcia-Herrera, R. Multidecadal variability of the summer length in Europe. *J. Clim.* **28**, 5375–5388 (2015).
28. Rutishauser, T., Luterbacher, J., Jeanneret, F., Pfister, C. & Wanner, H. A phenology-based reconstruction of interannual changes in past spring seasons. *J. Geophys. Res.* **112**, G04016 (2007).
29. Robinson, D. A. & Estilow, T. W. *NOAA CDR Program: NOAA Climate Data Record (CDR) of Northern Hemisphere (NH) Snow Cover Extent (SCE) Version 1.1* (NOAA National Climatic Data Center, 2012).
30. Menzel, A., Estrella, N. & Testka, A. Temperature response rates from long-term phenological records. *Clim. Res.* **30**, 21–28 (2005).

Acknowledgements

The authors thank the CNRM-Cerfacs group for the development of the CNRM-CM5 model and for producing the CMIP5 simulations. C.C. is indebted to L. Coquart and M.-P. Moine for making available the outputs at Cerfacs and J. Boé for helpful discussions. The figures were produced with the NCAR Command Language Software (<http://dx.doi.org/10.5065/D6WD3XH5>). Both C.C. and J.C. are supported by CNRS and by the MORDICUS grant under contract ANR-13-SENV-0002-01.

Author contributions

C.C. designed the study and performed the analyses. Both authors discussed the results and wrote the manuscript.

Additional information

Supplementary information is available in the [online version of the paper](#). Reprints and permissions information is available online at www.nature.com/reprints. Correspondence and requests for materials should be addressed to C.C.

Competing financial interests

The authors declare no competing financial interests.